Clays and Clay Minerals (2026), **74**, e11, 1–9
doi:10.1017/cmn.2026.10034

Original Paper

Cs^+ adsorption mechanisms on todorokite: an MD simulation study bridging atomistic and macroscopic scales

Juhyeok Kim and Kideok D. Kwon

Department of Geology, Kangwon National University, Chuncheon, Republic of Korea

Abstract

Understanding the long-term fate of radioactive cesium (^{137}Cs) following nuclear accidents requires mechanistic knowledge of its adsorption on soil minerals. Although todorokite is a major tectomanganate, the mechanisms governing Cs^+ adsorption at the trace levels typical of environmental contamination remain poorly understood. This study examined the concentration-dependent adsorption mechanisms of Cs^+ on todorokite through molecular dynamics (MD) simulations. Selectivity-coefficient calculations based on potential of mean force (PMF) profiles showed that sodium ions (Na^+) were energetically favored on external (100) and (010) todorokite surfaces, whereas this selectivity was reversed dramatically in favor of Cs^+ within tunnel nanopores. Na^+ encountered no significant kinetic barriers upon tunnel entry, but the interior was thermodynamically unfavorable; in contrast, Cs^+ faced high entry barriers but gained strong interior binding, resulting in slow desorption and high retention. Thus, the exceptional Cs^+ selectivity of todorokite arises from the contrasting energetic landscapes. Isotherm modeling of published experimental data, constrained by MD-derived equilibrium adsorption constants, suggested a concentration-dependent shift in dominant uptake sites, with intra-tunnel sites governing high-affinity adsorption at low Cs^+ concentrations, whereas external surfaces (where both inner- and outer-sphere complexes form) become dominant at higher Cs^+ concentrations.

Keywords: cesium adsorption; inner-sphere surface complexes; MD simulations; PMF free energy; todorokite; tunnel nanopores

(Received: 09 January 2026 UTC; revised: 10 April 2026 UTC; accepted: 17 April 2026 UTC)

Introduction

Soil minerals control the fate and transport of radioactive cesium (^{137}Cs) in subsurface environments primarily through interfacial adsorption processes. Consequently, understanding mineral–radionuclide interactions is critical for long-term environmental management following nuclear accidents (Ohnuki and Kozai, 2013; Benedicto et al., 2014; Chitrakar et al., 2014; Missana et al., 2014; Yu et al., 2017). Phyllosilicates such as clay minerals and micas have been investigated extensively as primary Cs^+ adsorbents, and Cs^+ interactions with their interlayers, frayed edges, and basal surfaces have been well characterized at the molecular scale (Bostick et al., 2002; Fan et al., 2014; Fuller et al., 2015; Mukai et al., 2016; Ruiz Pestana et al., 2017; Okumura et al., 2018; Li et al., 2021; Zhang et al., 2022). In contrast, although manganese (Mn) oxides exhibit extremely high sorption capacities for trace metals (Post, 1999; Dyer et al., 2000; Wegorzewski et al., 2020; Li et al., 2024), the underlying mechanisms of Cs^+ adsorption by Mn oxides, particularly tunnel-structured varieties such as todorokite, remain poorly understood.

Todorokite is a common tectomanganate featuring one-dimensional nanopores approximately 6.9 Å × 6.9 Å in size, formed by 3 × 3 Mn octahedral chains (Post and Bish, 1988; Post et al., 2003). This mineral provides unique structural features for selective metal retention (Dyer et al., 2000; Ohnuki and Kozai, 2013; Chitrakar et al., 2014; Yu et al., 2017; Zhang et al., 2020). Yu et al. (2017) systematically investigated Cs adsorption on todorokite across an exceptionally wide Cs^+ concentration range of 10^{-10} to 10^{-1} M using radiotracer techniques for low concentrations; they revealed that todorokite displays significant Cs^+ retention capacity comparable to that of phyllosilicates at low concentrations ($<10^{-8}$ mol L^{-1}), but negligible capacity at high concentrations. This concentration dependence suggests distinct adsorption mechanisms operating at different concentration regimes, which explains why todorokite has been overlooked in typical laboratory settings at high Cs^+ concentrations (~10^{-6} mol L^{-1}, ppm levels in solution). Given that ^{137}Cs concentrations in atmospheric fall-out were estimated at ~10 ppt levels within weeks of the Fukushima nuclear accident (Ohnuki and Kozai, 2013; Mukai et al., 2016), a fundamental mechanistic insight into Cs^+ adsorption at these dilute limits is essential for understanding the role of Mn oxides in controlling ^{137}Cs mobility.

However, elucidating the fundamental adsorption mechanisms of Cs^+ on todorokite surfaces remains experimentally challenging. Ion-exchange modeling studies have proposed two-site adsorption schemes (Yu et al., 2017; Min and Kim, 2022), but these assignments are derived solely from isotherm fitting, and do not provide crystallographic identities for the actual binding sites. Moreover, spectroscopic techniques such as Cs L_{III}-edge extended X-ray

Corresponding author: Kideok D. Kwon; Email: kkwon@kangwon.ac.kr

Cite this article: Kim J., & Kwon K.D. (2026). Cs^+ adsorption mechanisms on todorokite: an MD simulation study bridging atomistic and macroscopic scales. *Clays and Clay Minerals* **74**, e11, 1–9. https://doi.org/10.1017/cmn.2026.10034

© The Author(s), 2026. Published by Cambridge University Press on behalf of The Clay Minerals Society.

absorption fine structure spectroscopy require high Cs^+ concentrations (0.05–0.5 mol L^{-1}) to achieve sufficient signal-to-noise ratios to examine the molecular speciation of Cs^+ (Yu et al., 2017). As a result, such spectroscopic data contain overlapping signals of multiple heterogeneous species that prevent the deconvolution of adsorption mechanisms at trace Cs^+ concentrations. Thus, the molecular-scale interactions of Cs^+ with todorokite under environmentally relevant, low-concentration conditions remain unresolved.

The aim of the present study was to investigate the molecular-level mechanisms of Cs^+ adsorption on todorokite employing molecular dynamics (MD) simulations. MD simulation is a powerful tool for probing mineral–water interface structures at atomistic resolution and for extracting thermodynamic free energies that are difficult to obtain experimentally, thereby complementing spectroscopic and batch adsorption studies (Kerisit and Liu, 2014; Loganathan and Kalinichev, 2017; Ho and Criscenti, 2021; Li et al., 2021; Subramanian and Lammers, 2022; Kim et al., 2025). Previous MD studies on radionuclide adsorption have focused primarily on phyllosilicates, and MD simulation work for Mn oxides, particularly for tectomanganates, is lacking. In this study, todorokite tunnels and external surfaces were expected to provide concentration-dependent binding sites for Cs^+. MD simulations combined with free-energy calculations were used to systematically explore Cs^+ binding configurations at representative external (100) and (010) surfaces and within tunnel nanopores of todorokite, and to calculate equilibrium adsorption constants that were subsequently integrated into macroscopic isotherm models to assess the contributions of intra-tunnel and external-surface sites across concentration ranges.

Methods

Simulation models

The todorokite bulk structure was constructed as a 3 × 10 × 3 supercell based on an established experimental unit cell (Post et al., 2003). This model has an average oxidation state (AOS) of 3.73 for total Mn and a structural formula of $Mg^{2+}_{0.5}Na^{+}_{0.4}Ca^{2+}_{0.1}[Mn^{4+}_{4.4}, Mn^{3+}_{1.6}]\cdot 3.6H_2O$; additional structural details are provided elsewhere (Kim and Kwon, 2022). Mn^{3+} was substituted randomly at corner-sharing octahedral sites of Mn, following experimental evidence (Post and Bish, 1988). Todorokite typically occurs as rod-shaped crystals. To present external adsorption sites, two slab models representing (100) and (010) cleaved surfaces were created from the bulk structure. The (100) surface corresponds to the {100} lateral walls of exposed tunnels, whereas the (010) surface is a crystallographic plane that forms the interface between the internal tunnel space and the aqueous phase (Fig. 1). Each slab model included a 50 Å-thick water column perpendicular to the cleaved surface at both sides (see Fig. S1 in the Supplementary material). The water layer contained 1330–1340 H_2O molecules, corresponding to a density of 1 g cm^{-3}, with one Cs^+ or sodium ion (Na^+) plus a distant chloride (Cl^-) as the adsorbing ion-counterion pair. Terminal atoms of the slab models were hydroxylated to obtain charge neutral surfaces. However, hydroxylation does not compensate the structural charge arising from Mn^{3+} substitution in the tunnel framework. In bulk todorokite, this structural charge is balanced by tunnel cations, whereas for the (100) surface cleaving the crystal exposes Mn^{3+} octahedra and removes their compensating tunnel cations. To compensate the structural charge deficit, additional Cs^+/Na^+ ions were introduced to the (100) surface.

Crystallographically, the external (100) surface has heterogeneous adsorption sites arising from varied edge geometries and Mn^{3+} substitution patterns (see Fig. S2 in the Supplementary material). This surface consists of parallel rows of protruding Mn octahedra separated by terraces of three Mn octahedral chains, creating step-edge adsorption sites. These step edges are structurally asymmetric, forming an acute angle (Ac) on one side and an obtuse angle (Ob) on the other. Given the distinct adsorption energetics of these geometries, Ac and Ob sites were further classified according to the local Mn^{3+} distribution, as sites coordinated by a single Mn^{3+} octahedron (Ac1/Ob1) or by two Mn^{3+} octahedra (Ac2/Ob2). The specific location of Mn^{3+} is denoted by the suffixes 'b' for the base/terrace octahedron and 't' for the top/protruding octahedron (Fig. S2).

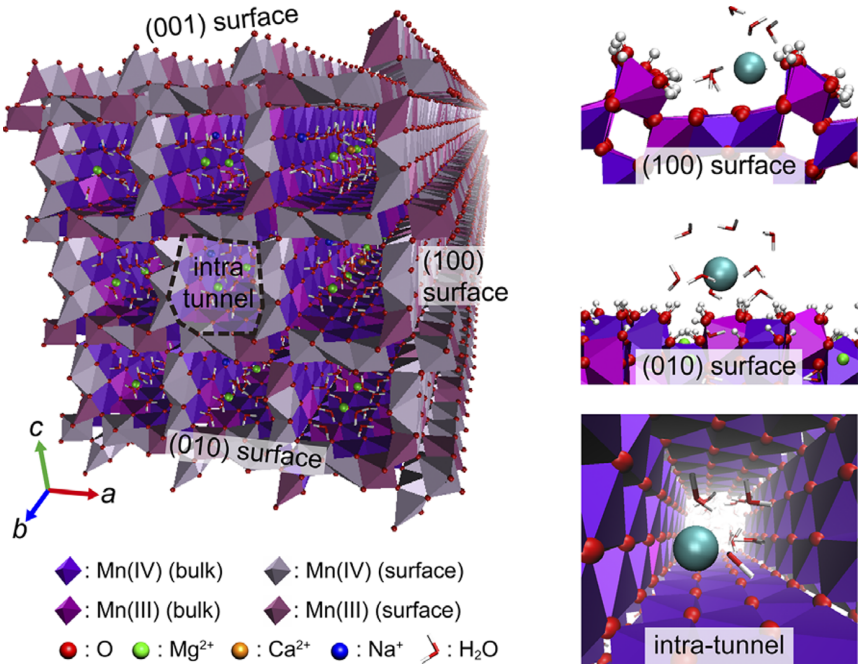


Figure 1. (Left) Perspective view of a todorokite model cleaved along the {010} and {100} planes. (Right) Representative MD simulation snapshots of adsorbed Cs^+ complexes. Only a fraction of the hydrating H_2O molecules is shown for visual clarity.

https://doi.org/10.1017/cmn.2026.10034 Published online by Cambridge University Press

MD simulations

All MD simulations were performed using GROMACS (Berendsen et al., 1995), with the velocity Verlet algorithm (Verlet, 1967) and a time step (Δt) of 1 fs in the numerical integration of the Newtonian equations of motion for all atoms. Interatomic interactions were described using the pair potentials of Newton and Kwon (2020) for the Mn oxide framework, the established potentials of Babu and Lim (2006), Smith and Dang (1994b), and Smith and Dang (1994a) for aqueous cations including Cs^+, and the SPC/E model for water (Berendsen et al., 1987) (see Table S1 in the Supplementary material). Lorentz–Berthelot combination rules were applied to calculate the interatomic energies of heterogeneous atom pairs (Allen and Tildesley, 2017). Partial charges of surface models were determined by the bond valence concept, as described in a previous study (Kim et al., 2022). Temperature was controlled using a Nose–Hoover thermostat (Shuichi, 1991). A cut-off radius of 10 Å was used for short-range interaction. The bond stretching and bending modes of water molecules (Ow) were constrained using the SETTLE algorithm (Miyamoto and Kollman, 1992). Each slab model was derived from the MD-simulated bulk structure of $Mg^{2+}_{0.5}Na^{+}_{0.4}Ca^{2+}_{0.1}[Mn^{4+}_{4.4}, Mn^{3+}_{1.6}]\cdot 3.6H_2O$ (Kim et al., 2022). The slab model systems underwent a 10 ns equilibration followed by a 50 ns production run in the number, volume, temperature (NVT) ensemble at 30 K. The last 30 ns of the MD trajectories were analyzed for structural analysis using GROMACS utilities and custom Python scripts. Coordination numbers were obtained by integrating the radial distribution functions up to the first-shell minimum. The simulation results were visualized using Visual Molecular Dynamics (Humphrey et al., 1996).

Free energy calculations

Potential of mean force (PMF) calculations (Roux and Simonson, 1999) were performed with umbrella sampling to predict the adsorption free energy of cations to todorokite surface (Kumar et al., 1992; Hub et al., 2010). For external surface adsorption, 60 umbrella windows were constructed by displacing a Cs^+ or Na^+ cation at 0.2-Å increments away from both the (100) and (010) surfaces. To ensure site-specific sampling of the heterogeneous sites (Table S2), the mobility of the target ion was confined within a 2.5-Å radius at each adsorption site. For the intra-tunnel sites, 260 reaction coordinate windows were generated, spanning the entire tunnel pathway from bulk water on one side to bulk water on the other side of the (010) slab model. Because pre-existing tunnel cations (Mg^{2+}, Ca^{2+}, Na^+) strongly hindered sampling of Cs^+/Na^+ configurations within the tunnel space (6.9 Å × 6.9 Å), the tunnel cations (but not water) were removed to avoid unrealistically large, effectively infinite repulsive forces and to obtain well-converged PMF profiles. In each window, a harmonic potential with a force constant of 377 kJ/mol/Å^2 was applied to constrain the cation along the reaction coordinate. This force constant ensured sufficient overlap between adjacent windows (Fig. S3). Each umbrella window (external surface and intra-tunnel) was sampled for 100 ns in the NVT ensemble at 300 K, with the sampling length selected based on convergence assessments for adequate statistical precision and reproducibility of the PMF profiles. PMF profiles were constructed from the simulation trajectories using the weighted histogram analysis method (Kumar et al., 1992; Hub et al., 2010). Statistical uncertainties were estimated from triplicate simulations and are expressed as a shaded band around the mean profile. Site-weighted average profiles were obtained by weighting the profile of each site by its relative abundance in the corresponding model (see Table S2 in the Supplementary material).

The selectivity coefficient (${}^{Cs}_{Na}K_{sel}$) of Cs^+ over Na^+ was derived from the equilibrium constants (K) of Cs^+ and Na^+ adsorption. For each cation, K was obtained by integrating the PMF profiles across the sampling space (Chialvo et al., 1995; Kerisit and Liu, 2014), as follows:

$$K = 2\pi \int_{r_{min}}^{r_{max}} r \cdot e^{-\beta W(r)} dr \quad (1)$$

where $W(r)$ is the PMF as a function of separation distance r between the ions and todorokite surfaces, and β is $1/k_BT$, with k_B representing the Boltzmann constant. The lower integration limit (r_{min}) at each adsorption site was defined as the shortest ion surface distance sampled in the PMF calculations, while the upper limit (r_{max}) corresponded to the distance at which the ion was effectively in bulk aqueous solution and the cumulative integral approached a constant value. The ion exchange reaction between Na-todorokite and Cs^+ is represented by:

$$Na^+ - \text{todorokite} + Cs^+_{aq} \rightarrow Cs^+ - \text{todorokite} + Na^+_{aq} \quad (2)$$

The selectivity coefficient was then evaluated as the ratio between K_{Cs} and K_{Na}:

$$\log_{Na}{}^{Cs}K_{sel} = \log K_{cs} - \log K_{Na}. \quad (3)$$

Results and Discussion

Adsorption on the (100) surface

MD simulations identified two dominant adsorption sites on the corrugated (100) surface: step edges and protruding octahedra (Fig. 2). However, site preferences differed substantially between Cs^+ and Na^+. The Cs^+ density distribution had a more delocalized and diffuse profile, whereas Na^+ had a more localized and fragmented density distribution. Structural analysis showed that Cs^+ ions atop protruding octahedra were coordinated by 3–4 surface oxygen atoms (Os) and 6–7 Ow at ~3.1 Å. At the step edges, Cs^+ ions were coordinated by 5 Os at ~3.0 Å and 5 Ow at 3.1 Å. In contrast, Na^+ ions along the step edges were coordinated by 3–4 Os and 2–3 Ow, with coordination distances of 2.4 Å; at the protruding octahedra, they were coordinated by 2 Os and 4 Ow, with comparable coordination distances.

Calculated PMF profiles for Cs^+ and Na^+ are shown in Fig. 3 as a function of distance from the surface reference position (surface O atomic plane at step edges, as shown in Fig. S1 in the Supplementary material). The profiles revealed two inner-sphere (IS) minima (Cs^+: ~2.5/5 Å and Na^+: ~2/4.5 Å) and one outer-sphere (OS) minimum (Cs^+: ~7.5 Å and Na^+: ~6.5 Å), with the precise positions of energy minima offset by their different ionic radii (Shannon, 1976). This positioning difference indicates that the smaller Na^+ remains closer to surface atoms, while the larger Cs^+ occupies more extended binding sites. Indeed, when free energy was pooled across all sites using site-weighted averaging (Fig. 3c), Na^+ exhibited more negative energy minima than Cs^+.

For Cs^+, the IS minima at 2.5 Å and 5 Å were associated with step edges and protruding octahedra, respectively, with OS complexes located above the protruding octahedra. At step edges, Ac-side sites (Ac1b, Ac1t) displayed unfavorable positive free energy, whereas Ob-side sites showed favorable negative energy (Fig. 3a; see also Fig. S4 in the Supplementary material). This energetics trend is

https://doi.org/10.1017/cmn.2026.10034 Published online by Cambridge University Press

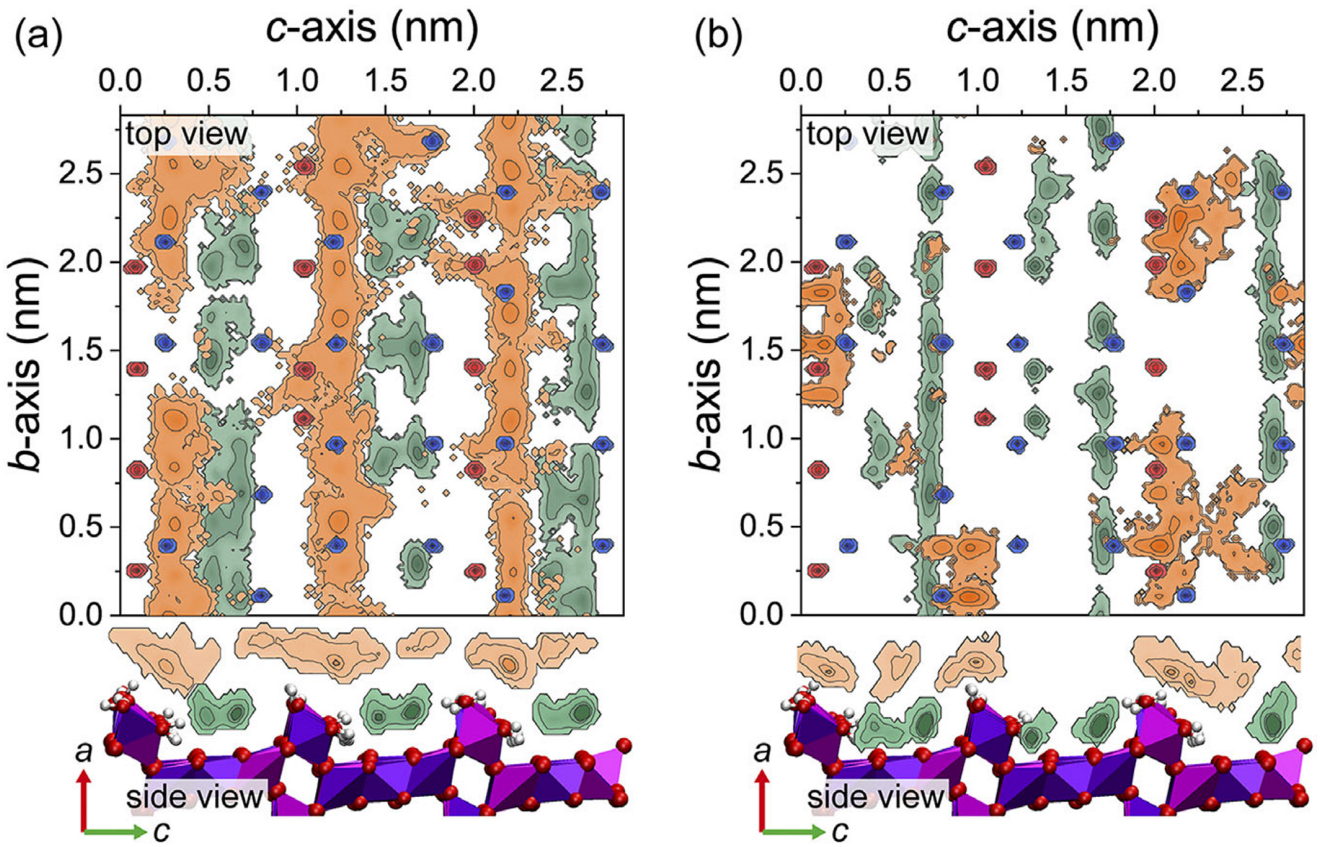


Figure 2. Atomic density profiles for (a) Cs^+ and (b) Na^+ adsorbed on the todorokite (100) surface. Orange and green contours indicate ion densities associated with protruding Mn octahedra at ~5 Å from the surface and with step edges sites at ~2.5 Å from the surface, respectively. Upper panels show side views of the corrugated surface structure. Small red and blue centric contours represent Mn^{3+} positions at the corner-sharing Mn octahedra.

consistent with the Cs^+ spatial distribution showing Ob-side dominance (Fig. 2a), probably due to incompatibility between the larger ionic radius of Cs^+ and the acute-angle Ac-side coordination environment. At the second minimum at 5 Å, Cs^+ favored the Ac side through double-edge sharing coordination with protruding octahedra, with minor corner-sharing on the Ob side (see Fig. S5 in the Supplementary material). Detailed coordination environments as a function of distance from the surface are shown in Fig. S6 (Supplementary material). Na^+ showed a similar pattern, with all IS minima at ~2 Å displaying negative free energy across the crystallographic binding sites and substantially lower energies on the Ob side (Fig. 3b; see also Fig. S7 in the Supplementary material), while at the second IS minimum (~4.5 Å), Na^+ also favored the Ac side, forming double-edge-sharing complexes (see Fig. S8 in the Supplementary material, for the coordination environments). These site-specific energetics were in good agreement with spatial density distributions obtained from MD simulations (Fig. 2b), supporting the correspondence between occupied positions and energetically favorable sites.

Adsorption on the (010) surface

The (010) surface provided relatively planar binding sites overlying Mn^{3+} and Mn^{4+} octahedra (Fig. 1; see also Table S2 in the Supplementary material). Cs^+ showed distinct free energy minima at 4 and 6 Å, corresponding to the formation of IS and OS complexes, respectively (Fig. 4a). Similarly, Na^+ formed IS and OS complexes at 3.5 and 5 Å (Fig. 4b). Na^+ exhibited site-specific energy minima dependent on the Mn oxidation state (Mn^{3+} *vs* Mn^{4+}), whereas Cs^+ appeared insensitive to the oxidation state. For Cs^+, IS complexes were coordinated by 2–3 Os and 6–7 Ow, while OS complexes were coordinated by 8 Ow (see Fig. S9 in the Supplementary material); both complexes exhibited similar Cs–O bond distances of ~3.1 Å, consistent with the small free energy difference and relatively shallow energy wells characteristic of comparable IS and OS states for Cs^+ (Fig. 4a). In contrast, for Na^+, IS complexes showed much more negative free energy than OS complexes (Fig. 4b); IS complexes were coordinated by 2 Os and 4 Ow at the distance of ~2.4 Å, while OS complexes were coordinated by 6 Ow at comparable distances (see Fig. S10 in the Supplementary material).

According to the site-weighted average PMF profiles, Na^+ adsorption was more favorable than Cs^+ adsorption on the todorokite (010) surface (Fig. 4c). The Na^+ PMF profile exhibited two distinct thermodynamic features compared with Cs^+: a higher-energy barrier between OS and IS states and a deeper IS energy minimum. These features indicate that IS complexation is thermodynamically more stable for Na^+ than for Cs^+. In contrast, the Cs^+ PMF profile showed comparable adsorption energy between OS and IS complexes, separated by relatively small energy barriers. This shallow-energy landscape would facilitate transitions between the two binding modes on nanosecond

https://doi.org/10.1017/cmn.2026.10034 Published online by Cambridge University Press

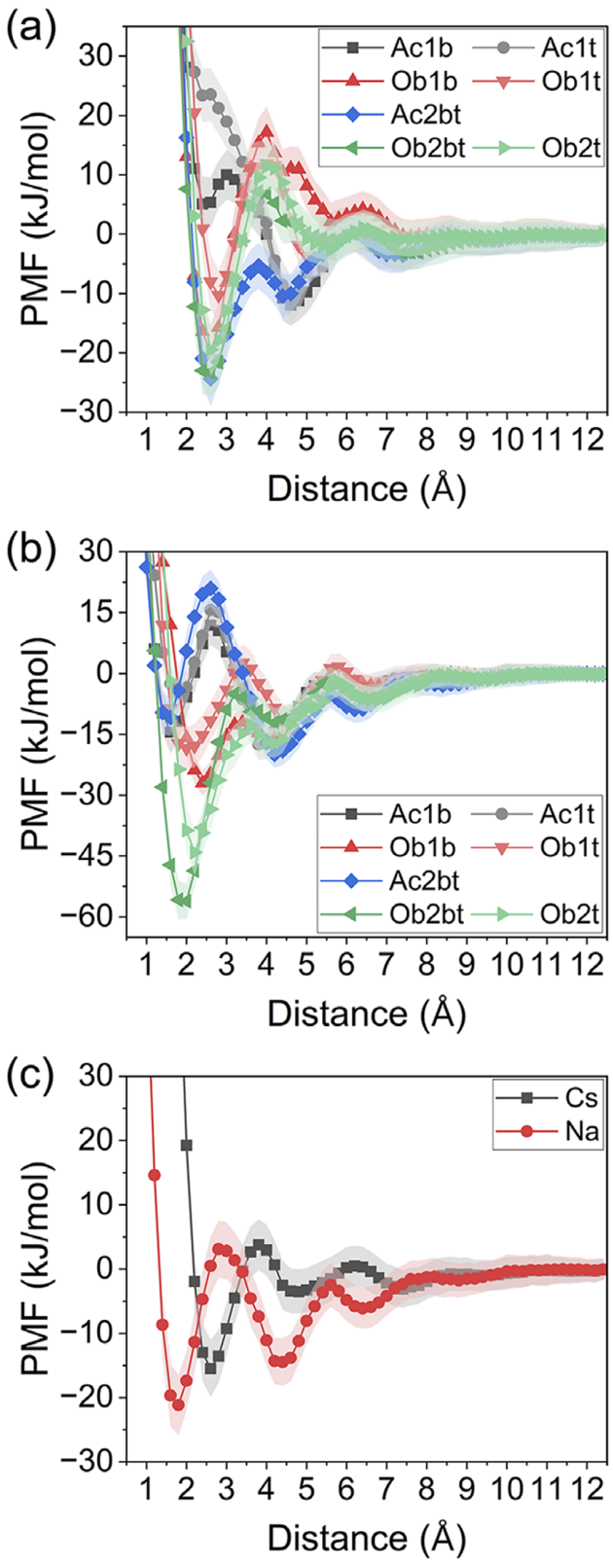


Figure 3. Potentials of mean force (PMF) profiles for (a) Cs^+ and (b) Na^+ adsorption at candidate binding sites on the todorokite (100) surface (see Fig. S2 for site notation), shown as a function of distance from the surface for each site. (c) Site-weighted average PMF profiles comparing Cs^+ and Na^+ adsorption on the (100) surface.

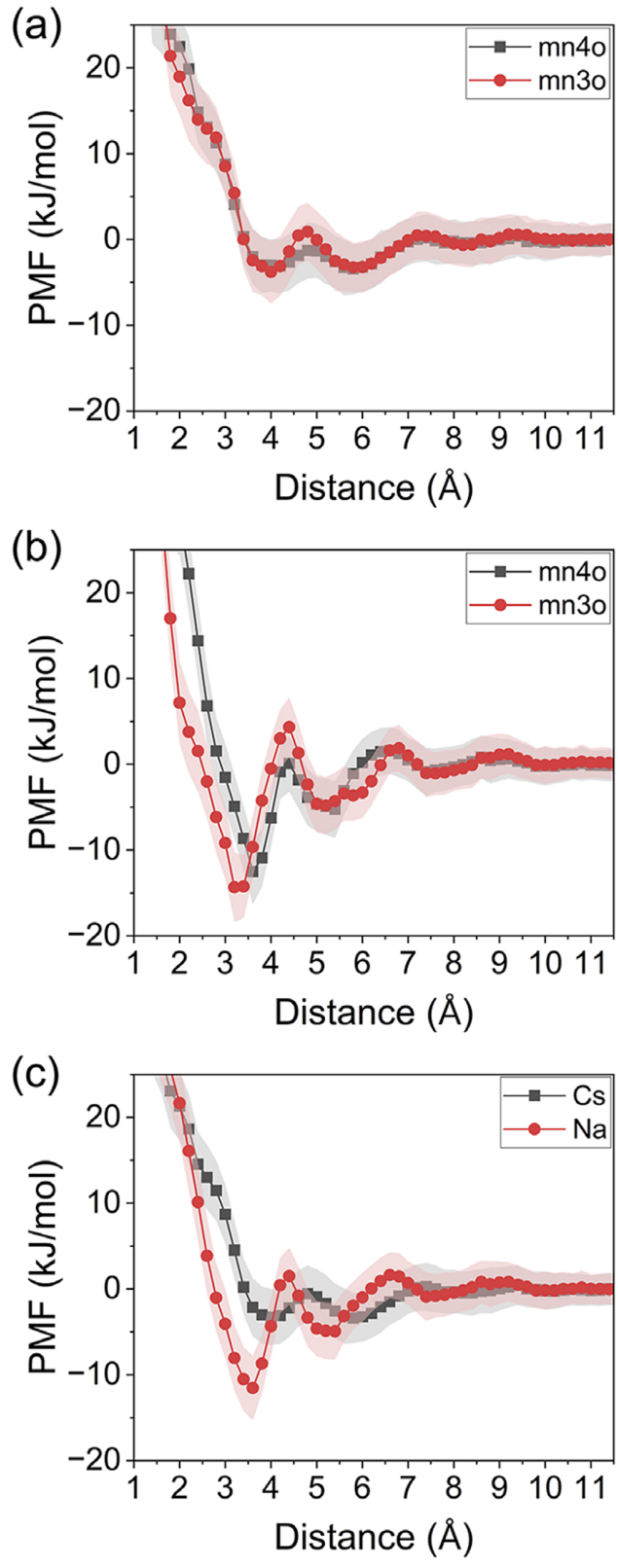


Figure 4. Potentials of mean force (PMF) profiles for (a) Cs^+ and (b) Na^+ adsorption on the todorokite (010) surface as a function of distance from the surface, and (c) site-weighted average PMF profiles comparing the two cations.

https://doi.org/10.1017/cmn.2026.10034 Published online by Cambridge University Press

timescales, consistent with the dynamic exchanges between IS and OS complexes observed in previous MD simulations (Kim et al., 2022).

Adsorption within tunnels

PMF profiles within the tunnel structure revealed trends opposite to those observed on external surfaces (Fig. 5), with Cs^+ strongly preferred over Na^+ in the tunnel nanopores. The PMF energies oscillated within tunnels as a function of cation position along the tunnel axis (from –28 to 0 Å; Fig. 5) due to periodic variation in the adsorption sites. Cs^+ consistently exhibited stable binding energy (negative PMF values relative to bulk water), whereas Na^+ displayed energy barriers (positive PMF values). This reversal in selectivity indicates that Cs^+ ions are thermodynamically stable within the tunnel nanopores, while Na^+ ions are unstable relative to the bulk aqueous phase. Local PMF profiles may be influenced by short-range Mn^{3+} ordering in the tunnel framework, which was not considered in the present study; however, such effects on the PMF of individual ions are expected to be minor compared with the PMF difference between Cs^+ and Na^+. The nearly symmetric PMF profiles for both cations further indicate adequate sampling convergence, with equivalent transition barriers for entry and exit from the tunnel space.

Todorokite tunnels have three primary adsorption sites: corner sites adjacent to corner-sharing Mn octahedra, edge sites along edge-sharing Mn octahedral chains, and center sites deep within the tunnel framework (see Fig. S11 in the Supplementary material). Cs^+ exhibited strong site selectivity, with ~85% of occupied corner sites as IS complexes and only 3% of occupied center sites as OS complexes. Structurally, coordination environments reflect this selectivity. Cs^+ IS complexes at corner sites were coordinated by 5–6 Ow and 5–6 Os; at edge sites, coordination involved 3–5 Os, whereas Cs^+ OS complexes were coordinated exclusively by 7–8 Ow (Fig. 6a). The PMF profiles showed that energy minima corresponded precisely to corner site occupancy, while energy maxima aligned with edge and center sites. This clear correspondence between favorable free energy sites and observed Cs^+ positions indicates that the todorokite tunnel framework provides highly selective binding sites for Cs^+. In contrast, Na^+ exhibited fundamentally different tunnel behavior, with no clear site preference. Approximately 40% of Na^+ formed OS complexes at center sites (coordinated by 5.8 Ow), while 40% formed IS complexes at corner sites (coordinated by 2 Os and 4 Ow) (Fig. 6b). Critically, the Na^+ positions showed little correspondence with the PMF energy landscape, indicating that the tunnel provides no energetically preferred site for Na^+. This contrast suggests that the todorokite tunnel provides efficient adsorption sites for Cs^+, but not for the smaller Na^+ ion.

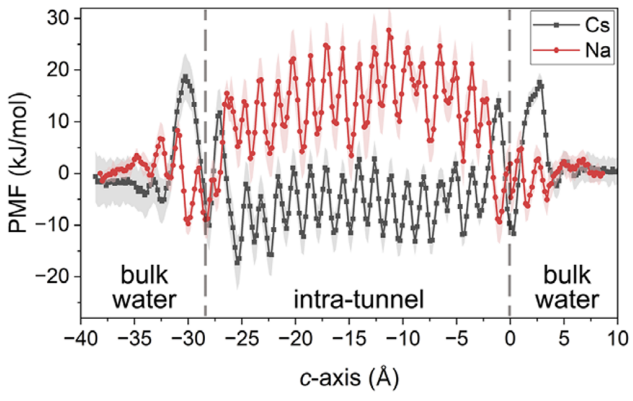


Figure 5. Potentials of mean force (PMF) profiles for Cs^+ and Na^+ within a todorokite tunnel structure as a function of cation position along the tunnel axis. The tunnel interior ranges from –28 Å to 0 Å, with bulk-water regions located at positions below –28 Å and above 0 Å (see Fig. 1).

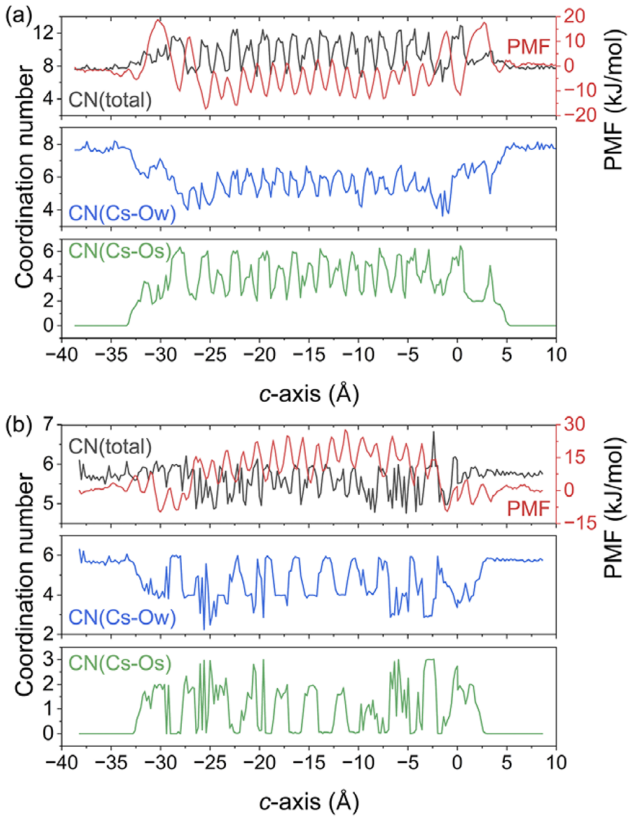


Figure 6. Coordination numbers of (a) Cs^+ and (b) Na^+ with water oxygen atoms (Ow) and tunnel surface oxygen atoms (Os) as a function of cation position along the todorokite tunnel axis. Positions below –28 Å and above 0 Å represent the bulk water phase. PMF profiles are overlain for correlation analysis with coordination environment.

Significant free energy barriers were found in the Cs^+ PMF profile at the tunnel interface (positions –33 to –28 Å and 0 to +5 Å; Fig. 5), particularly at entry and exit points. In contrast, the Na^+ PMF profile showed negligible barriers at equivalent positions. These results imply that Cs^+ intercalation and deintercalation must overcome substantial energy barriers, whereas Na^+ migration is largely unimpeded. This contrasting feature may be attributable to the geometric constraints of the rigid todorokite tunnel (6.9 Å × 6.9 Å) relative to the hydrated ion sizes. The larger hydrated Cs^+ ion (hydrated diameter: 6.2 Å) experiences significant steric hindrance at the interface, such that partial dehydration is required to traverse the tunnel entrance. This dehydration process is evident in the coordination profiles; *CN* (Cs-Ow) decreased from ~8 in bulk water to ~6 at the tunnel entrance, and further to 4–5 upon entry into the tunnel interior (Fig. 6a). Concurrently, *CN*(Cs-Os) increased from 0 to 2–4 at the interface. Thus, the significant energy barriers for Cs^+ represent the energetic cost of the simultaneous desolvation and structural rearrangement required to coordinate with tunnel Os. In contrast, the more compact hydrated Na^+ (hydrated diameter: 4.8 Å) fitted

https://doi.org/10.1017/cmn.2026.10034 Published online by Cambridge University Press

through the tunnel entrance without requiring significant dehydration, maintaining most of its hydration shell throughout the entry process.

The high-energy barriers at the interface, complemented by deep, free energy wells inside tunnels, have profound implications for Cs^+ retention. Because energy barriers control entry kinetics and interior wells determine the thermodynamic stability of intercalated species, todorokite tunnels are equipped with a dual Cs^+ mechanism that enables effective sequestration of Cs^+ within the tunnels. Experimental studies have shown that todorokite exhibits significantly lower Cs^+ desorption rates (50–70%) compared with layered birnessite and illite (> 95%) under similar conditions (Chitrakar et al., 2014; Yu et al., 2017; Murota et al., 2020). According to the PMF features, the interfacial barriers would slow desorption, while the deep interior wells would keep accumulated Cs^+ in a thermodynamically favorable state, which explains the pronounced Cs^+ retention of tectomanganates observed at experimental time scales.

Concentration-dependent adsorption mechanisms

Equilibrium constants derived based on site-weighted average PMF profiles for cation adsorption are listed in Table 1. The calculated log ${}^{Cs}_{Na}K_{sel}$ values indicate strong Cs^+ selectivity in tunnel sites, whereas Cs^+ and Na^+ compete for external sites. Yu et al. (2017) proposed two dominant adsorption sites on todorokite: a high-affinity (T1) site saturating at very low concentrations and a low-affinity (T2) site dominating uptake at higher concentrations. Although the precise crystallographic identities of these sites have not been resolved experimentally, the close agreement between the MD-derived selectivity coefficients and experimental values (Table 1) indicates that T1 and T2 sites probably correspond to intra-tunnels and external (010)/(100) surface sites, respectively.

However, fitting published isotherm data with the MD-derived K_{Cs} values (Fig. 7) demonstrated that the crystallographic sites represented in the present simulations reproduced Cs^+ uptake only up to $[Cs^+] < \sim 10^{-4}$ mol L^{-1}, and failed to capture the full high-concentration regime of the experiments. A Langmuir model using the MD intra-tunnel constant ($\log K_{Cs} = 7.6$) successfully reproduced the low-concentration proportion of the Yu et al. (2017) isotherm ($[Cs^+] < \sim 10^{-8}$ mol L^{-1}) (Fig. 7a), whereas external-surface constants ($\log K_{Cs} = 4.6$ or 5.2) matched the data only over the intermediate concentration range of $[Cs^+] \approx 10^{-8}$–10^{-4} mol L^{-1}. Min and Kim (2022) reported a two-site model that did not include sub-ppb concentrations; the MD external surface constants reproduced their data only between 10^{-8} and 10^{-4} mol L^{-1}, underfitting at higher concentrations (Fig. 7b). These high-concentration discrepancies suggest the involvement of additional adsorption sites that are not fully represented in the idealized models. Such sites probably reflect heterogeneous surface terminations and/or confined pore environments arising from oxide particle aggregation.

Table 1. Calculated equilibrium constants (log K) for Cs^+ and Na^+ adsorption and selectivity coefficients (log ${}^{Cs}_{Na}K_{sel}$) at todorokite surfaces

	Current MD simulations			EXP*	
	Intra-tunnel	(010) surface	(100) surface	T1	T2
log K_{Cs}	7.6±0.4	4.6±0.1	5.2±0.1	NR	NR
log K_{Na}	4.2±0.1	4.9±0.2	5.8±0.1	NR	NR
log ${}^{Cs}_{Na}K_{sel}$	3.4±0.3	–0.3±0.2	–0.6±0.1	4.2	–0.6

*EXP = experimental results (Yu *et al.*, 2017); NR = not reported.

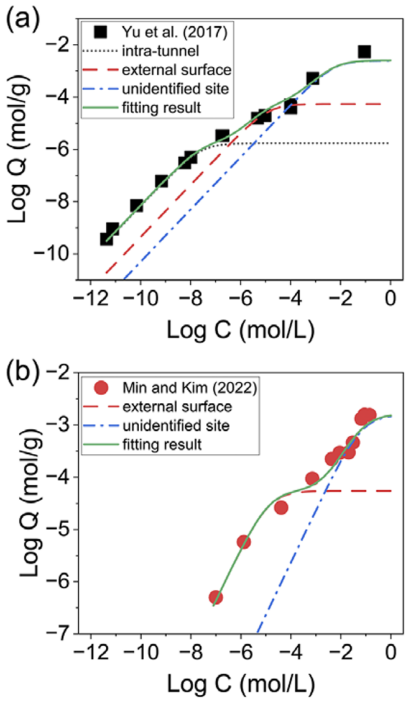


Figure 7. Comparison of experimental Cs^+ adsorption isotherm data for todorokite from (a) Yu et al. (2017) and (b) Min and Kim (2022), with Langmuir model fits using MD-predicted equilibrium constants for intra-tunnel and external-surface sites (Table 1).

The multi-site Langmuir approach informed by the MD simulations enabled one-to-one mapping between crystallographic adsorption sites and macroscopic adsorption behavior across varying Cs^+ concentrations (Table S3): intra-tunnel sites governing low-concentration uptake (ppb levels), external surface sites dominating the intermediate-concentration regime (ppm levels), and unidentified sites accounting for adsorption at much higher concentrations. These findings demonstrate the value of integrating molecular simulations with macroscopic adsorption models for interpreting complex experimental behavior.

Conclusions

Long-term radionuclide immobilization following nuclear accidents is a critical challenge in environmental and nuclear-waste management. Because radioactive fallout deposits ^{137}Cs at sub-ppb levels, understanding its adsorption and desorption behavior under dilute concentrations is essential for risk assessment. Nevertheless, investigating Cs^+ adsorption mechanisms at environmentally relevant concentrations remains challenging for conventional experimental approaches. In this study, MD simulations revealed that Cs^+ predominantly forms IS complexes within todorokite tunnels, whereas both IS and OS complexes coexist on external surfaces. PMF calculations combined with isotherm comparison further revealed a concentration-dependent shift in Cs^+ binding from intra-tunnels at trace concentrations to external surfaces at higher loadings. Mechanistically, the tunnel framework imposes substantial energy barriers that kinetically inhibit Cs^+ desorption to bulk water. These results demonstrate that the unique 3 × 3 todorokite tunnel framework selectively stabilizes Cs^+ at trace

https://doi.org/10.1017/cmn.2026.10034 Published online by Cambridge University Press

concentrations through partially desolvated IS coordination, whereas external surfaces provide less selective, reversible adsorption at higher adsorbate levels. These findings identify todorokite as a potentially important geochemical scavenger for long-term ^{137}Cs immobilization following nuclear contamination events.

Supplementary material. The supplementary material for this article can be found at https://doi.org/10.1017/cmn.2026.10034.

Author contributions. Juhyeok Kim: Conceptualization, Methodology, Software, Formal Analysis, Investigation, Writing – Original Draft. Kideok D. Kwon: Conceptualization, Resources, Supervision, Writhing – Review & Editing.

Data availability statement. The data that support the findings of this study are available from the corresponding author upon reasonable request.

Financial support. This research was supported by the Basic Science Research Program through the National Research Foundation of Korea (NRF) (RS-2024-00333926), and the computations were performed using the supercomputing resources of the Korea Institute of Science and Technology Information (KSC-2025-CRE-0030). J.K. acknowledges scholarship support from the Korea Ministry of Education (RS-2023-00273714).

Competing interests. The authors declare no competing interests.none.

References

Allen, M.P., & Tildesley, D.J. (2017). *Computer Simulation of Liquids*. Oxford University Press, Oxford, UK.

Babu, C.S., & Lim, C. (2006). Empirical force fields for biologically active divalent metal cations in water. *Journal of Physical Chemistry A*, *110*, 691–699.

Benedicto, A., Missana, T., & Fernández, A.M. (2014). Interlayer collapse affects on cesium adsorption onto illite. *Environmental Science & Technology*, *48*, 4909–4915.

Berendsen, H., Grigera, J., & Straatsma, T. (1987). The missing term in effective pair potentials. *Journal of Physical Chemistry*, *91*, 6269–6271.

Berendsen, H.J., van der Spoel, D., & van Drunen, R. (1995). GROMACS: a message-passing parallel molecular dynamics implementation. *Computer Physics Communications*, *91*, 43–56.

Bostick, B.C., Vairavamurthy, M.A., Karthikeyan, K., & Chorover, J. (2002). Cesium adsorption on clay minerals: an EXAFS spectroscopic investigation. *Environmental Science & Technology*, *36*, 2670–2676.

Chialvo, A., Cummings, P., Cochran, H., Simonson, J., & Mesmer, R. (1995). Na^+-Cl^- ion pair association in supercritical water. *Journal of Chemical Physics*, *103*, 9379–9387.

Chitrakar, R., Makita, Y., & Sonoda, A. (2014). Cesium adsorption by synthetic todorokite-type manganese oxides. *Bulletin of the Chemical Society of Japan*, *87*, 733–739.

Dyer, A., Pillinger, M., Newton, J., Harjula, R., Möller, T., & Amin, S. (2000). Sorption behavior of radionuclides on crystalline synthetic tunnel manganese oxides. *Chemistry of Materials*, *12*, 3798–3804.

Fan, Q., Tanaka, M., Tanaka, K., Sakaguchi, A., & Takahashi, Y. (2014). An EXAFS study on the effects of natural organic matter and the expandability of clay minerals on cesium adsorption and mobility. *Geochimica et Cosmochimica Acta*, *135*, 49–65.

Fuller, A.J., Shaw, S., Ward, M.B., Haigh, S.J., Mosselmans, J.F.W., Peacock, C.L., Stackhouse, S., Dent, A.J., Trivedi, D., & Burke, I.T. (2015) Caesium incorporation and retention in illite interlayers. *Applied Clay Science*, *108*, 128–134.

Ho, T.A. & Criscenti, L.J. (2021) Molecular-level understanding of gibbsite particle aggregation in water. *Journal of Colloid and Interface Science*, *600*, 310–317.

Hub, J.S., De Groot, B.L., & Van Der Spoel, D. (2010). g_wham – a free weighted histogram analysis implementation including robust error and autocorrelation estimates. *Journal of Chemical Theory and Computation*, *6*, 3713–3720.

Humphrey, W., Dalke, A., & Schulten, K. (1996). VMD: visual molecular dynamics. *Journal of Molecular Graphics*, *14*, 33–38.

Kerisit, S., & Liu, C. (2014). Molecular dynamics simulations of uranyl and uranyl carbonate adsorption at aluminosilicate surfaces. *Environmental Science & Technology*, *48*, 3899–3907.

Kim, H., Kim, J., Hyun, S.P., & Kwon, K.D. (2022). Toward a mechanistic understanding of cesium adsorption to todorokite: a molecular dynamics simulation study. *Journal of Hazardous Materials*, *436*, 129250.

Kim, J., & Kwon, K.D. (2022). Tunnel cation and water structures of todorokite: insights into metal partitioning and isotopic fractionation. *Geochimica et Cosmochimica Acta*, *333*, 153–165.

Kim, J., Hwang, H., Lee, J.-Y., & Kwon, K.D. (2025). Mineral surface-specific nanoplastic adsorption: insights from quartz crystal microbalance experiment and molecular modeling simulations. *Science of the Total Environment*, *975*, 179231.

Kumar, S., Rosenberg, J.M., Bouzida, D., Swendsen, R.H., & Kollman, P.A. (1992). The weighted histogram analysis method for free-energy calculations on biomolecules. I. The method. *Journal of Computational Chemistry*, *13*, 1011–1021.

Li, F., Yin, H., Zhu, T., & Zhuang, W. (2024). Understanding the role of manganese oxides in retaining harmful metals: insights into oxidation and adsorption mechanisms at microstructure level. *Eco-Environment & Health*, *3*, 89–106.

Li, X., Tang, L., Liu, N., Chang, Q., & Zhang, J. (2021). Coupling of adsorption site and cation ratio regulates the adsorption of Cs^+ and Na^+ at the surface of clay mineral. *Applied Clay Science*, *209*, 106121.

Loganathan, N., & Kalinichev, A.G. (2017). Quantifying the mechanisms of site-specific ion exchange at an inhomogeneously charged surface: case of Cs^+/K^+ on hydrated muscovite mica. *Journal of Physical Chemistry C*, *121*, 7829–7836.

Min, S., & Kim, Y. (2022). Adsorption characteristics of cs and cation selectivity of todorokite. *Colloids and Surfaces A: Physicochemical and Engineering Aspects*, *650*, 129652.

Missana, T., Benedicto, A., García-Gutiérrez, M., & Alonso, U. (2014). Modeling cesium retention onto Na-, K- and Ca-smectite: effects of ionic strength, exchange and competing cations on the determination of selectivity coefficients. *Geochimica et Cosmochimica Acta*, *128*, 266–277.

Miyamoto, S., & Kollman, P.A. (1992). SETTLE: an analytical version of the SHAKE and RATTLE algorithm for rigid water models. *Journal of Computational Chemistry*, *13*, 952–962.

Mukai, H., Hirose, A., Motai, S., Kikuchi, R., Tanoi, K., Nakanishi, T.M., Yaita, T., & Kogure, T. (2016) Cesium adsorption/desorption behavior of clay minerals considering actual contamination conditions in fukushima. *Scientific Reports*, *6*, 21543.

Murota, K., Tanoi, K., Ochiai, A., Utsunomiya, S., & Saito, T. (2020). Desorption mechanisms of cesium from illite and vermiculite. *Applied Geochemistry*, *123*, 104768.

Newton, A.G., & Kwon, K.D. (2020). Classical mechanical simulations of layer- and tunnel-structured manganese oxide minerals. *Geochimica et Cosmochimica Acta*, *291*, 92–109.

Ohnuki, T., & Kozai, N. (2013). Adsorption behavior of radioactive cesium by non-mica minerals. *Journal of Nuclear Science and Technology*, *50*, 369–375.

Okumura, M., Kerisit, S., Bourg, I.C., Lammers, L.N., Ikeda, T., Sassi, M., Rosso, K.M., & Machida, M. (2018). Radiocesium interaction with clay minerals: theory and simulation advances post–fukushima. *Journal of Environmental Radioactivity*, *189*, 135–145.

Post, J.E. (1999). Manganese oxide minerals: crystal structures and economic and environmental significance. *Proceedings of the National Academy of Sciences*, *96*, 3447–3454.

Post, J.E., & Bish, D.L. (1988). Rietveld refinement of the todorokite structure. *American Mineralogist*, *73*, 861–869.

Post, J.E., Heaney, P.J., & Hanson, J. (2003). Synchrotron x-ray diffraction study of the structure and dehydration behavior of todorokite. *American Mineralogist*, *88*, 142–150.

Roux, B., & Simonson, T. (1999). Implicit solvent models. *Biophysical Chemistry*, *78*, 1–20.

Ruiz Pestana, L., Kolluri, K., Head-Gordon, T., & Lammers, L.N. (2017). Direct exchange mechanism for interlayer ions in non-swelling clays. *Environmental Science & Technology*, *51*, 393–400.

Shannon, R.D. (1976). Revised effective ionic radii and systematic studies of interatomic distances in halides and chalcogenides. *Acta Crystallographica, Section A: Crystal Physics, Diffraction, Theoretical and General Crystallography*, *32*, 751–767.

Shuichi, N. (1991). Constant temperature molecular dynamics methods. *Progress of Theoretical Physics Supplement*, *103*, 1–46.

Smith, D.E., & Dang, L.X. (1994a). Computer simulations of cesium–water clusters: do ion–water clusters form gas-phase clathrates? *Journal of Chemical Physics*, *101*, 7873–7881.

Smith, D.E., & Dang, L.X. (1994b). Computer simulations of NaCl association in polarizable water. *Journal of Chemical Physics*, *100*, 3757–3766.

Subramanian, N., & Lammers, L.N. (2022). Thermodynamics of ion exchange coupled with swelling reactions in hydrated clay minerals. *Journal of Colloid and Interface Science*, *608*, 692–701.

Verlet, L. (1967). Computer 'experiments' on classical fluids. I. Thermodynamical properties of Lennard-Jones molecules. *Physical Review*, *159*, 98–103.

Wegorzewski, A.V., Grangeon, S., Webb, S.M., Heller, C., & Kuhn, T. (2020). Mineralogical transformations in polymetallic nodules and the change of Ni, Cu and Co crystal-chemistry upon burial in sediments. *Geochimica et Cosmochimica Acta*, *282*, 19–37.

Yu, Q., Ohnuki, T., Kozai, N., Sakamoto, F., Tanaka, K., & Sasaki, K. (2017). Quantitative analysis of radiocesium retention onto birnessite and todorokite. *Chemical Geology*, *470*, 141–151.

Zhang, C., Liu, L., Dai, Y., Zhu, K., Liu, Z., & Jia, H. (2022). Molecular dynamics simulations of exchange behavior of radionuclides into montmorillonite: unraveling the dynamic processes and microscopic structures. *Applied Clay Science*, *226*, 106579.

Zhang, H., Zhu, J., Ma, L., Kang, L., Hu, M., Li, S., & Chen, Y. (2020) Electrochemical adsorption of Cs^+ ions on H-todorokite nanorods. *ACS Omega*, *5*, 1062–1067.

https://doi.org/10.1017/cmn.2026.10034 Published online by Cambridge University Press